IEEE Photonics Journal
An IEEE Photonics Society Publication

Ultracompact Optical Hybrid Based on Standing Wave Integrated With Graphene-Based Photodetector for Coherent Detection

Volume 10, Number 6, December 2018

Jing Xu
Yanli Zhao
Ke Wen
Junjie Tu

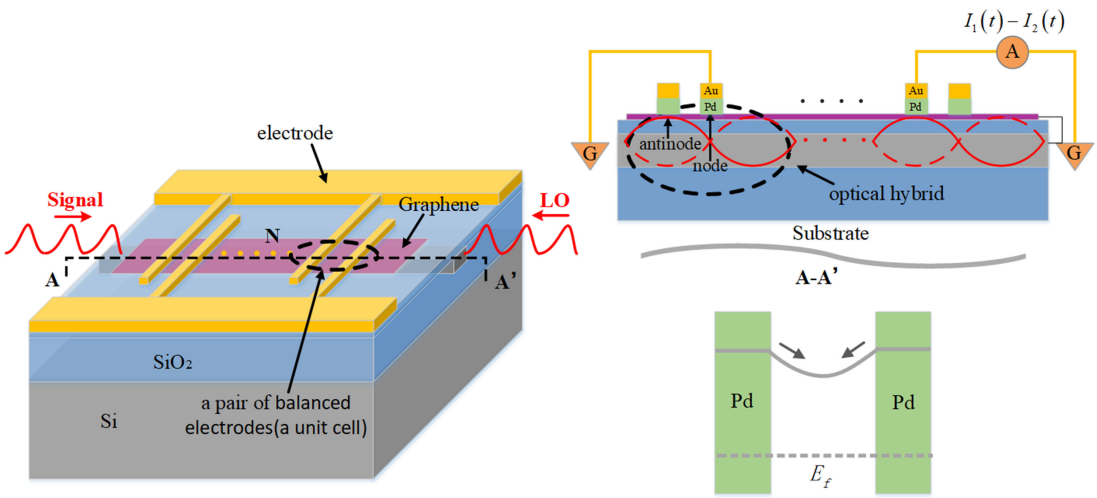

DOI: 10.1109/JPHOT.2018.2863695
1943-0655 © 2018 CCBY

IEEE photonics SOCIETY
IEEE

Ultracompact Optical Hybrid Based on Standing Wave Integrated With Graphene-Based Photodetector for Coherent Detection

Jing Xu, Yanli Zhao, Ke Wen, and Junjie Tu

Wuhan National Laboratory for Optoelectronics, Huazhong University of Science and Technology, Wuhan 430074, China

DOI:10.1109/JPHOT.2018.2863695

Manuscript received June 1, 2018; revised July 25, 2018; accepted July 31, 2018. Date of publication August 6, 2018; date of current version November 29, 2018. Corresponding author: Yanli Zhao (e-mail: yanlizhao@mail.hust.edu.cn).

Abstract: In this paper, we propose a novel scheme to integrate an optical hybrid based on standing wave with graphene photodetector (GPD). Different from optical hybrids based on multimode interference (MMI) couplers, the proposed optical hybrid can be miniaturized by constructing a standing wave field in a silicon strip waveguide. The waveguide-integrated GPD with symmetric electrodes is adopted as an ultrafast self-differential photodetector (SDPD), instead of conventional balanced-photodetectors (BPDs) based on p-i-n photodiodes in a coherent receiver. By placing two sysmmetric interdigitated electrodes of the SDPD at nodes and antinodes of the standing wave, it is convenient to realize the integration of the proposed optical hybrid with the graphene-based SDPD, which can effectively reduce the complexity of a coherent receiver and meet the future demand for wide bandwidth. The finite-difference time-domain method was used to calculate optical absorption for demonstrating operation feasibility. Finally, device bandwidth and effective responsivity have been discussed. In theory, our scheme would provide a feasible way to realize a high-speed compact coherent receiver.

Index Terms: Integrated optics devices, coherent detection, optical hybrid, graphene photodetector.

1. Introduction

Coherent detection, one of the most promising detection techniques, has been commonly used for high-speed data transfer due to its high sensitivity, high spectral efficiency, and the possibility of electronic compensation of signal impairments [1], [2]. With steady growth and improvement of global communication networks, the demand for increased bandwidth is ever present, and large-scale integration requires high-yield integration processes and ultra-small footprint components. The development of integrated coherent receivers is an attractive step towards the miniaturization and high-speed application. Such integration of coherent receivers have been realized in InP photonic integrated circuits (PICs) [3]–[5], silicon PICs [6]–[9], and hybrid PICs [10]–[13]. They are usually designed as integrated MMI optical hybrids connected to PIN photodiodes pairs which are used for balanced detection. Integrated coherent receivers with waveguide photodetectors operating at 100 G/s and beyond have been a technical and commercial success, however, there are still many technical challenges to reach higher bandwidth. On the other hand, for MMI optical hybrids, they

are limited by fabrication tolerance and usually not compact. Moreover, some integrated coherent receivers have high fabrication costs, facing the challenge of integration with existing electronics and photonics platforms. Hence, developing high-speed photodetectors (PDs) and advanced photonic integration based on mature complementary metal oxide semiconductor (CMOS) fabrication process is strongly needed for future on-chip coherent systems.

Recently, the application potential of graphene for integrated photonics has been recognized due to its alluring optoelectronic properties and easiness to integrate as 2D material [14], [15]. Various promising optoelectronic devices based on graphene have been proposed [14]–[19]. Among them, graphene photodetectors (GPDs) have attracted strong interest for their exceptional physical properties, especially an ultrafast response across a broad spectrum [20]–[27]. The most widely used concept for graphene photodetectors is based on the photovoltaic charge separation at a graphene-metal interface, where a shift in Fermi's energy is introduced by the metal. It is reported that the GPDs can operate bias-free with zero dark current and the high intrinsic bandwidth can potentially reach up to ~500 GHz [21]–[23].

In this work, we propose a novel scheme to integrate an optical hybrid based on standing wave with graphene-based SDPD. It can also be regarded as a graphene-based standing wave detector for coherent detection. There are two special designs different from the integrated coherent balanced receivers reported in previous works [3]–[13]. First, different from the optical hybrids mainly realized using the MMI couplers based on traveling wave interference [3]–[13], [28], the optical hybrid in our scheme is based on the coherent mechanism of standing wave, where it can generate the constructive interference light at antinodes and the destructive interference light at nodes of standing wave. Second, the waveguide-integrated GPD is used as an ultrafast SDPD, instead of the conventional BPDs based on PIN photodiodes in a coherent receiver. Particularly, compared to the typical GPDs with asymmetric electrodes, the GPD with symmetric electrodes (we call them balanced-electrodes in this paper) can be used for self-balanced detection. By placing the balanced-electrodes of the SDPD at nodes and antinodes of the standing wave pattern, the optical waveguide mode couples to the graphene layer through evanescent field and then the output current of the SDPD is the differential current between the photocurrent from antinodes and from nodes. By this way, it is easy to realize the integration of the optical hybrid with the graphene-based SDPD. It's a promising way to effectively reduce the complexity and the size of a coherent receiver, quite different from MMI optical hybrids connected to BPDs. FDTD simulations were held on the SDPD by defining a unit cell as a pair of balanced electrodes whose length is of only 0.5 μm. In addition, we define the effective responsivity (R_{eff}) as the ratio between the photogenerated current (I_{ph}) and the signal power (P_S). By increasing the unit cells, the graphene layers absorb additively, leading to a higher responsivity, but with the increase in size and the decrease of bandwidth of the device. In the case of the device with 10 unit cells, the bandwidth is estimated to be160 GHz and the length is around 5 μm. And the effective responsivity changes in the range of 1 A/W to 4 A/W when the ratio of the local oscillator power (P_{LO}) to P_S is from 20 dB to 30 dB.

2. Operation Principle and Structure Design

Before discussing our design, we present a general theoretical description of the coherent detection system. Fundamental coherent detection utilizes a180-degree optical hybrid with one 2 × 2 MMI to mix the incoming signal with the local oscillator (LO), into a pair of BPDs to detect the amplitude and the phase of signal, as shown in Fig. 1.

In an ideal homodyne detection, the output currents of the two well matched PDs are given as followed [29]

$$I_1(t) = \frac{1}{2}R\left\{P_{LO}(t) + P_S(t) + 2\sqrt{P_{LO}(t)P_S(t)}\cos\left[\varphi(t)\right]\right\} \quad (1)$$

$$I_2(t) = \frac{1}{2}R\left\{P_{LO}(t) + P_S(t) - 2\sqrt{P_{LO}(t)P_S(t)}\cos\left[\varphi(t)\right]\right\} \quad (2)$$

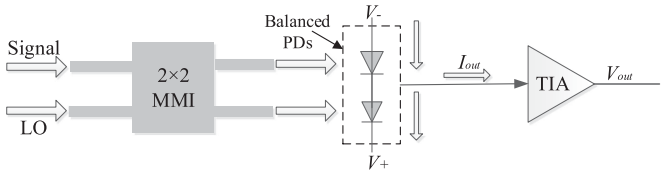

Fig. 1. The schematic diagram of the coherent receiver, where TIA represents trans-impedance amplifier.

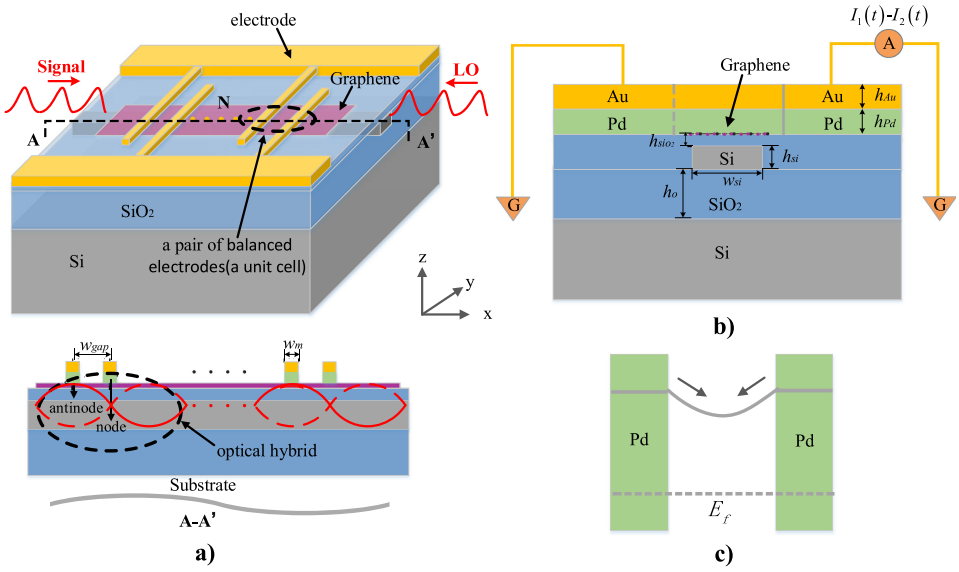

Fig. 2. (a) Top: Three-dimensional schematic illustration of the graphene-based SDPD. Bottom: Schematic of the metal electrodes placement. The red line represents stable standing wave field, which can function as optical hybrid. (b) Cross section view of the SDPD. (c) The graphene band profile with the palladium-doped balanced-electrodes. The dotted line represents the Fermi level. Device parameters: $w_{si} = 600$ nm, $h_{si} = 220$ nm, $h_o = 3\mu$m, $h_{sio2} = 10$ nm, $h_{Au} = 20$ nm, $h_{Pd} = 20$ nm, $w_{gap} = 230$ nm, $w_m = 40$ nm.

where R is the responsivity of the two PDs, $P_{LO}(t)$ and $P_S(t)$ represent the powers of LO and received signal, respectively, $\varphi(t)$ is the phase difference between signal and LO. As shown in Fig. 1, the injected current of TIA is the difference between the output currents $I_1(t)$ and $I_2(t)$. Since the direct current (DC) of each side of the two well-matched PDs is identical, the differential current output by BPDs is then given by

$$I_{out}(t) = 2R\sqrt{P_{LO}(t)P_S(t)}\cos[\varphi(t)] \tag{3}$$

Here, we explore the use of high bandwidth, few-layers of GPD as ultrafast SDPD instead of the BPDs in a traditional coherent receiver. In a simple approach, we design the GPD geometries whose graphene sheet contacted by two metal contacts that serve as source and drain electrodes. The schematic configuration of the proposed device is illustrated in Fig. 2, which can realize the same function as Fig. 1 except for TIA. The geometry of this graphene-based SDPD with N pairs of balanced-electrodes (N unit cells) is similar to that of traditional metal-semiconductor-metal (MSM) detectors. The photonic base layer consists of SOI stripe waveguides with 600 nm wide and 220 nm thick on an insulator with 3 μm buried oxide. In order to make a planarized surface, the silicon waveguide is backfilled with silica, and another thin 10 nm thick SiO_2 layer is deposited on the planarized surface to electrically isolate the graphene layer from the underlying SOI waveguide. The optical waveguide mode couples to the graphene layer through the evanescent field, leading to optical absorption and photon-generated carriers. The interdigitated balanced-electrodes made

of palladium/gold (20/20 nm in thickness) are on surface of the graphene in the stripe waveguide region. The corresponding electrodes are connected to the contact pads located on opposite sides of the waveguide, with separations of 3.5 μm from the edges of the waveguide, respectively, to ensure that the optical modes of the waveguide remain undisturbed by the contact pads [23]. The graphene band profile with palladium-doped balanced-electrodes is shown in Fig. 2(c).

Considering the factors of remaining undisturbed by the dark current and easiness to demonstrate our scheme, the SDPD is supposed to work under zero-bias operation. Details about GPDs working at zero bias have been discussed previously [22], [23]. In the GPDs demonstrated previously [22], the internal (built-in) electric fields, which are responsible for the separation of the photo-generated carriers, only exist in narrow regions ($\sim$200 nm) adjacent to the electrode/graphene interfaces, where charge transfer between the metal and graphene leads to band bending. But due to the absence of an acceptable electric field in the bulk graphene sheet, photo-excitation is followed by rapid carrier recombination, without any contribution to the external photocurrent. Thus, multiple interdigitated electrodes are used to create of a greatly enlarged, high E-field, light-detection region. However, for the uniform light field, if the two electrodes consist of the same metal, the built-in electric field profile is symmetric in the channel between two neighbouring interdigitated electrodes, the photocurrents generated around these two electrodes have the same magnitude, but opposite polarity, accordingly the total photocurrent is always close to zero. Thus the GPDs demonstrated previously usually adopt asymmetric electrodes scheme, such as two different metals to create different metal/graphene junction (one with high work-function and the other one with low work-function [22]), or asymmetric electrodes (one is close enough from the waveguide to efficiently separate the photoexcited electron-hole pairs and the other is far enough from the edge of the waveguide to limit optical absorption [23]).

In our work, combining with the non-uniformity of standing wave field distribution, we adopt a symmetric metallization scheme to realize efficient self-balanced detection. By taking advantage of a standing wave formed by two counter-propagating and coherently modulated signal and LO from the opposite sides of the SOI waveguide, an alternating field distribution of bright antinode and dark node is shaped in the strip waveguide. The graphene sheet placed in the path of the coherent light beams experiences different electric field intensity, depending on its position within the standing wave field profile. Through calculation and analysis, the light intensity at an antinode and a node of the standing wave pattern satisfies the relationship deduced from Eq. (1) and Eq. (2), respectively, whereby it can function as a 180-degree optical hybrid. At the same time, a symmetric metallization electrode scheme is designedly adopted to utilize the mirror symmetry of the internal electric-field profile in graphene channels. By placing narrow strip electrodes above the graphene sheet at the nodes and antinodes regions, the optical absorption of graphene is minimized at nodes and maximized at antinodes. The equal part of photocurrents (DC part in $I_1(t)$/ $I_2(t)$ expression) generated in constructive interference regions and destructive interference regions are opposite polarity, without any contribution to the external photocurrent, thus the final output photocurrent is differential current. Then the GPD with balanced-electrodes can realize self-differential photodetection, which can function as the BPDs in conventional coherent receiver.

3. Physical Model

Here, graphene is treated as an anisotropic material whose out-of plane conductivity $\sigma_\perp$ is different from the in-plane conductivity σ. The in-plane conductivity of graphene consists of intraband and interband contributions, which can be derived within the random phase approximation [30], [31],

$$\sigma_{//} = \sigma_{\text{intra}} + \sigma_{\text{inter}} = \frac{i8\sigma_0}{\pi}\frac{E_{th}}{E_{ph}+iE_s}\ln\left[2\cosh\left(\frac{E_f}{2E_{th}}\right)\right] + \sigma_0\left[\frac{1}{2}+\frac{1}{\pi}\tan^{-1}\left(\frac{E_{ph}-2E_f}{2E_{th}}\right)-\frac{i}{2\pi}\ln\frac{\left(E_{ph}+2E_f\right)^2}{\left(E_{ph}-2E_f\right)^2+4E_{th}^2}\right] \quad (4)$$

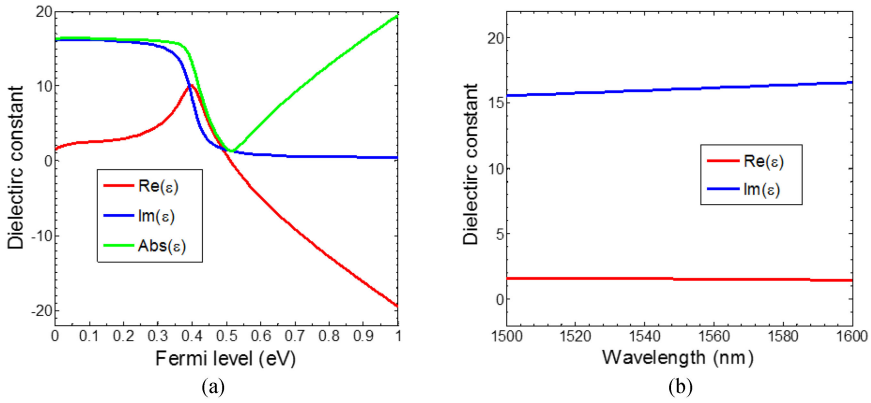

Fig. 3. (a) Calculated dielectric constant of graphene (real part, imaginary part and magnitude) versus Fermi energy at $\lambda = 1550$ nm. (b) Dielectric constant of graphene versus light wavelength under chemical potential of graphene $\mu = 0$ eV.

where $\sigma_0 = e^2\pi/(2h)$ is the universal conductivity of graphene (e is the charge of an electron, and h is the Planck constant), $E_{th} = k_B T$ is thermal energy in eV (k_B is the Boltzmann constant and T is the temperature), E_f is the Fermi energy (that is chemical potential μ) of graphene in eV, $E_{ph} = hc/\lambda$ is photon energy in eV, and $E_s = h/(2\pi\tau)$ is the scattering energy in eV for the scattering time τ.

The dielectric function $\varepsilon(\mu)$ can be obtained from the complex optical conductivity of graphene written by

$$\varepsilon_{//}(\mu) = 2.5 + \frac{i\sigma_{//}(\mu)}{\omega\varepsilon_0\Delta} \tag{5}$$

where $\Delta = 0.34$nm is the thickness of monolayer graphene [30], ε_0 is the permittivity of vacuum, and the out-of plane permittivity is assumed to be $\varepsilon_\perp(\mu) = 2.5$.

The dielectric constant of graphene is calculated as a function of the Fermi energy E_f for a wavelength of $\lambda = 1550$ nm, $T = 300$ K, $\tau = 0.1$ps, as shown in Fig. 3(a). Fig. 3(b) shows the dielectric constant of graphene as a function of incident light wavelength when the chemical potential of graphene is 0 eV.

The FDTD method (using Lumerical FDTD Solutions software) is used for simulations. Optical properties of other materials are modeled using the default Palik refractive index data available in the Lumerical material database [32]–[34]. The boundary condition is Perfectly Matched Layer (PML). The incident illumination is mode source set in the forward and backward X direction of the waveguide, which represents the signal and the LO, respectively. P_{LO} is equal to P_S by default setting. The optical wavelength is set to 1550 nm.

Fig. 4(a), (b) show the standing wave optical field distributions for both TE and TM modes on xy-plane parallel to the graphene sheet of the device without balanced-electrodes. The gap between a node and an antinode (w'_{gap}) equals to $\lambda/(4n_{eff})$, where n_{eff} is the effective index of the waveguide mode. Since n_{eff} for TE and TM modes in the SOI waveguide are different, w'_{gap} for both modes are accordingly different. Taking into account the factors of electric field intensity and fabrication tolerance, we choose TM mode as the light source for our design and simulation. The standing wave field distributions are depicted in Fig. 4(c), (d) for TM mode on xy-plane parallel to the graphene sheet of the device with a pair of balanced-electrodes. From Fig. 4(c) and (d), it can be found that when the phase difference between the signal and the LO changes from 0° to 180°, the positions of the node and the antinode are swapped, resulting in the reverse polarity for output differential current. The interdigitated balanced-electrodes are designed with a width (w_m) of 40 nm and a gap (w_{gap}) of 230 nm. Moreover, if using a low refractive index waveguide integrated graphene photodetector, e.g., silicon nitride waveguide-integrated graphene photodetector [35] or

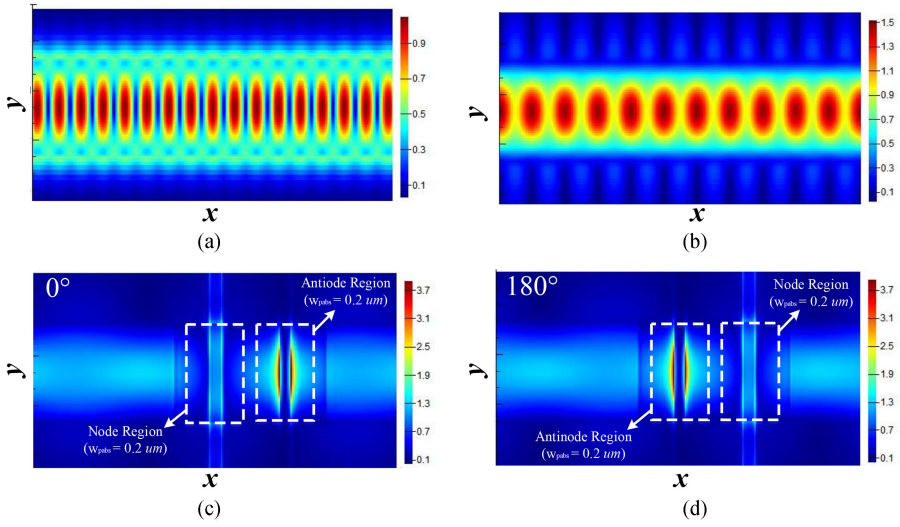

Fig. 4. The electric field |E| map parallel to the graphene sheet of the device (a) without balanced-electrodes for TE mode; (b) without balanced-electrodes for TM mode; (c) with a pair of balanced-electrodes under 0° phase difference for TM mode.; (d) with a pair of balanced-electrodes under 180° phase difference for TM mode. The white dashed rectangle boxes represent the effective absorption regions set to 200 nm × 600 nm × 1 nm (dx × dy × dz).

slot waveguide-integrated graphene photodetector [36], such that the gap between the nodes and antinodes could be further increased to prevent the interaction between the electrodes.

Furthermore, from Fig. 4, it can be found that obvious interference fringes are formed in graphene sheets of the devices with/without balanced-electrodes. Compared to device without electrodes, for the device with balanced-electrodes, at the antinode regions, there is obvious electric field enhancement at the metal edge, but a low electric field in the metal finger region. We argue that there may be localized surface plasmon resonance effect at the metal edge, accordingly leading to higher optical absorption, and a low electric field in the metal finger region is due to the optical absorption induced by metal. According to the simulation, the metal loss is less than 0.8% of incident light power at an antinode and less than 0.4% of incident light power at a node for 1550 nm wavelength. In [37], it's shown that the photocurrent at the graphene–metal interface is a combination of the photo-thermoelectric effect due to light absorption in graphene and the thermoelectric effect due to light absorption in the metal contacts, where the former dominates above 600 nm wavelength. Hence, we focus on performing simulations to calculate the optical absorption induced by graphene sheet.

4. Simulation Results and Discussion

The most important criterions of PDs are responsivity, 3 dB bandwidth and dark current. In this work, the GPD is used to allow for large bandwidth, and the operation of zero bias can lead to zero dark current. Besides, the SDPD with self-balanced characteristic can effectively reduce the noise. Thus our investigation concentrates on the responsivity, which is also the major limitation for the applications of GPDs. Taking into account that both the photovoltaic effect (the built-in field) and the photo-thermoelectric effects contribute to the photocurrent [37], [38], it's not easy to make a suitable model of photocurrent for our scheme by simulation and it's not the main issue we focus on in this paper. Since photocurrent generated from both photovoltaic and photo-thermoelectric effects are related to the optical absorption of graphene, we simulate the optical absorption of graphene, which is proportional to the responsivity, to demonstrate the operation feasibility. Simulation results also confirm the operation feasibility under various circumstances.

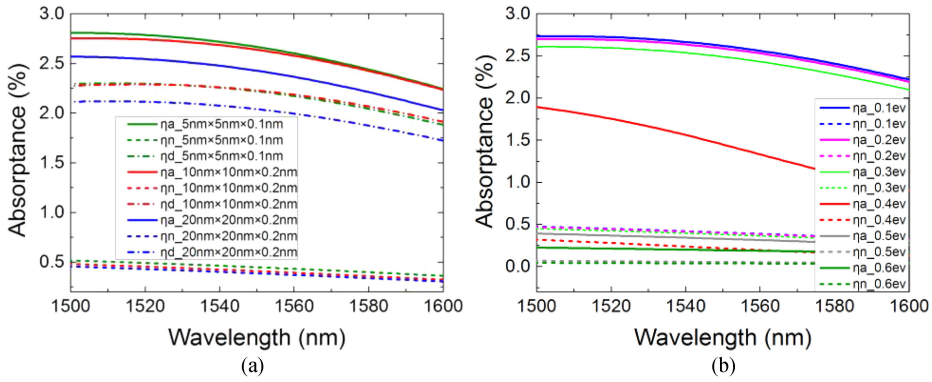

Fig. 5. (a) The absorptance of a unit cell versus light wavelength for the same structure with varied mesh dimensions (chemical potential of graphene is 0 eV). (b) The absorptance of a unit cell versus light wavelength under different chemical potentials of graphene. The solid lines denote the absorptance of an antinode region, the dashed lines denote the absorptance of a node region and the dash-dotted lines denote the differential absorptance.

4.1 Numerical Absorption Results

We would discuss the graphene induced absorption properties in this configuration and plot the absorption curves. The results are mainly obtained from the SDPD with a pair of balanced-electrodes and the footprint of graphene for a unit cell is 500 nm $\times$ 600 nm $\times$ 1 nm (dx $\times$ dy $\times$ dz). Due to the characteristic discussed above that in GPDs, photo-generated carriers which can contribute to the output photocurrent only exist in narrow regions ($\sim$200 nm) adjacent to the electrode/graphene interfaces and in our design, the distance between the neighbouring interdigitated balanced-electrodes is also around 200 nm, the 3D rectangle power monitors (each dimensions is 200 nm $\times$ 600 nm $\times$ 1 nm) are used to record the optical absorption of graphene sheet at the nodes and antinodes regions, respectively. We use the absorptance η, which is the ratio between the absorbed light power and the total incident light power, to describe the optical absorption efficiency. And the differential absorptance η_d is defined as the difference of the absorptance between the antinodes and nodes regions. The absorptance η and the differential absorptance η_d can be given by

$$\eta = \frac{p_{abs}}{p_{in}} = \frac{\iiint_{V_{abs}} \frac{1}{2}\omega \cdot imag(\varepsilon)\left|\overline{E}\right|^2 dV}{P_{source}} \tag{6}$$

$$\eta_d = \eta_a - \eta_n \tag{7}$$

where ω is the angular optical frequency, imag(ε) is the imaginary part of the dielectric permittivity of graphene,$\overline{E}$ is the electric field intensity, $P_{source} = P_{LO} + P_S$ is the source power, and V_{abs} is the volume of the absorption region. η_a and η_n are the absorptance of antinodes regions and nodes regions, respectively. Frist, as Fig. 5(a) shows, the simulation precision analysis is done by using varied mesh dimensions (dx $\times$ dy $\times$ dz) of graphene layer.

To make balance the simulation precision with computing time, we set the mesh dimensions of garphene layer to be 10 nm $\times$ 10 nm $\times$ 0.2 nm, corresponding to the red curve. Since the red curve and green curve (5 nm $\times$ 5 nm $\times$ 0.1nm) almost overlap, the absolute error of absorptance can be estimated to below 0.5% from infinitely dense mesh.

As we know, one of the important properties of graphene is gate-variable optical conductivity. Since the conductivity of graphene can be dynamically tuned by applying drive voltages, which will change the carrier density and accordingly shift the Fermi level of graphene, the absorption range can be modified by changing the chemical potentials of graphene using an external gate field. This gate-controllability characteristic of graphene is always utilized to design the graphene field-effect transistor. Here, if various levels of gate voltages are applied, the graphene-based device can be a tunable device. Fig. 5(b) plots the absorption spectra of graphene at an antinode region and a node

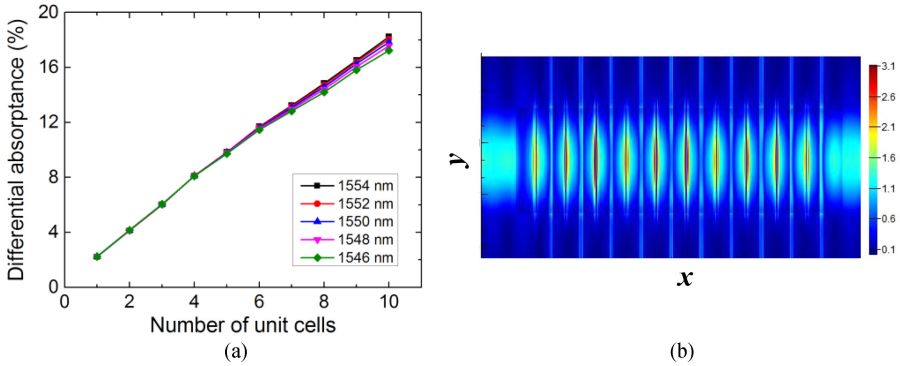

Fig. 6. (a) The differential absorptance of the device with different number of unit cells. (b) The electric field |E| map parallel to the graphene sheet of the device with 10 unit cells.

region as a function of light wavelength under different chemical potentials of graphene. According to the simulation, we can see that the absorptance of an antinode region is more than 2.6% and the absorptance of a node region is only 0.4% at 1550 nm wavelength within the graphene chemical potential of 0 $\sim$ 0.3 eV. However, when the chemical potential is 0.4 eV, the absorptance of an antinode region drops sharply to half of the absorption peak and continues to drop to less than 0.5% when the chemical potential is more than 0.5 eV. The results agree with the trend of the dielectric constant of graphene as a function of the chemical potentials, as shown in Fig. 3(a). In fact, due to the non-uniform optical absorption between the graphene channel, the position of the Fermi level with respect to the Dirac point is non-uniform in our scheme. However, since the change of Fermi level introduced by the non-uniform optical absorption is small and the optical absorption of graphene within the chemical potential of 0 $\sim$ 0.3 eV is almost coincident, as shown in Fig. 5(b), we can use the model of constant chemical potentials for the whole graphene sheet in the absorption simulations to demonstrate the operation feasibility. In an extreme approach, where we set the graphene chemical potential of 0.3 eV at an antinode region and 0 eV at a node region, the simulation result shows that the absorptance of an antinode region is 2.4% and the absorptance of a node region is 0.4% at 1550 nm wavelength, and the η_{d} can also keep $\sim$2% from 1550 nm to 1600 nm wavelength.

Although the absorption peak efficiency of an antinode region is less than 3%, considering the absorption region of an antinode is only nanoscale (200 nm $\times$ 600 nm $\times$ 1 nm $=$ 1.2 $\times$ 10^5nm^3) and the graphene's relatively low optical absorption ($\sim$2.3% for single layer graphene [20]), there is a significant light absorption enhancement here by taking advantage of standing wave effect and surface plasmon resonance effect. In addition, for the antinode region and the node region, the graphene inherently exhibits nearly flat absorption spectra over a wide wavelength range of 100 nm, respectively, owing to its ability to absorb light over a broad wavelength range and the characteristic of the device with nanoscale structure.

A significant advantage of our scheme is to realize the self-balanced coherent detection using simple structure. Double increase in the number of metal fingers means a linear increase in the number of unit cells, accordingly leading to a higher optical absorption. We further investigate the performance of the SDPD with multiple pairs of balanced-electrodes on absorption. Due to computational resource limitations, we simulate the configurations whose number of unit cells is from 1 to 10. From Fig. 6(a), it is shown that the absorptance increases almost linearly with the number of unit cells, satisfying theoretical expectation. In addition, it can be found that as the unit cells increases, the device's absorption characteristics are more sensitive to wavelength changes. When the number of unit cells is 10, the total η_{d} achieves 18%.

Although higher quantity of unit cells can lead to a higher responsivity of the SDPD, considering the size of the device increases and the bandwidth of the device decreases due to the increased capacitance, the number of unit cells should be reasonably chosen. Moreover, there are a lot of researches to enhance the optical absorption of graphene, such as by introducing hybrid

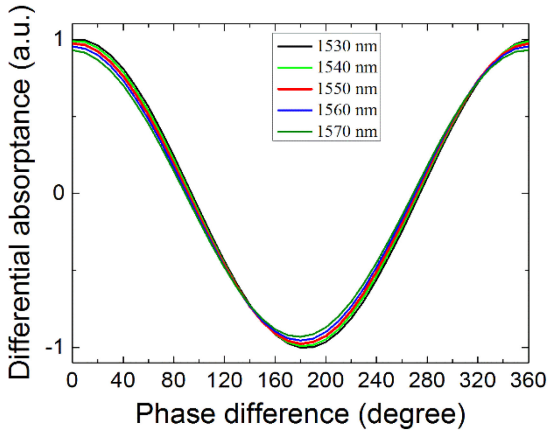

Fig. 7. The normalized differential absorptance versus phase mismatch under different light wavelength.

graphene-quantum dot [39], integration with microcavity [40] or coupling graphene with plasmonic nanostructures [41]. These researches can be adopted to further improve the responsivity of our device in future work.

4.2 Discussion for Phase Mismatch

In practical long-haul coherent systems, the phase of the LO might be uncorrelated with the phase of the signal and the phase mismatch is compensated electronically. So it's valuable to study the output characteristics of the device when the phase mismatch occurs between the signal and the LO. We simulate and demonstrate the normalized differential absorptance, which is proportional to the output current of the device, by taking into account that the phase mismatch can be completely random from 0 up to 360 degrees, as shown in Fig. 7.

From Fig. 7, it is found when the phase difference changes from 0 to 360 degrees, the normalized differential absorptance coincides with the cosine change. The results indicate that the output characteristics of the device are similar to that of the balanced detectors in traditional coherent receivers, satisfying Eq. (3) discussed above. Hence the optical phase-locked loops technology and the digital signal processing technology in traditional coherent receivers can also be applied to the proposed scheme [42], [43].

4.3 Discussion for Bandwidth and Responsivity

The bandwidth of PDs is limited by the carrier transit time between the electrodes and the RC delay. As we know, graphene has a huge carrier mobility and hence the bandwidth limited by the carrier transit time is always high for GPDs.

In most conventional photodiodes, large external bias directly applied to the photodetecting area and its complete depletion are essential for fast and efficient photodetection [44]. However, the internal fields can be used to produce an ultrafast photocurrent response in GPDs owing to the high carrier transport velocity existing even at zero bias. According to the Ref. [21], the transit time limited bandwidth can be given by

$$f_{tr} = 3.5/2\pi t_{tr} \tag{8}$$

where t_{tr} is the transit time through the photodetection region. If we assume that the carrier, under a chemical potential of graphene of 0 eV can travel at a Fermi velocity of 10^6m/s [15], it would take only 0.2 ps for the carriers to travel out of the ~200 nm current generation region. Thus, a value of f_{tr} of 2.8 THz is obtained.

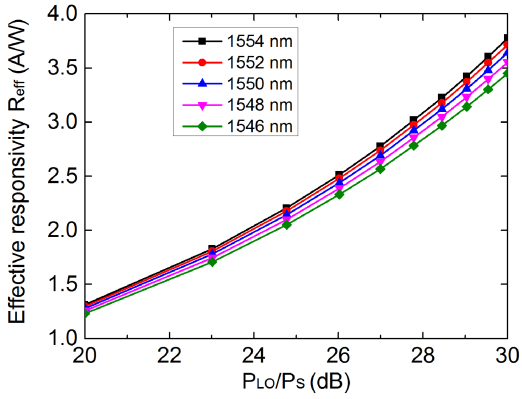

Fig. 8. The effective responsivity of the device with 10 unit cells versus the P_{LO}/P_S ratio.

The RC limited bandwidth f_{RC} is given by

$$f_{RC} = 1/(2\pi RC) \tag{9}$$

Here, the pad capacitance is ignored. According to the measurement data in [21], we can estimate the capacitance of the area of a unit graphene sheet ($0.5\mu m \times 0.6\mu m$) at zero bias is 2 fF. Assuming the load resistance R of 50 Ω, the RC limited bandwidth for a unit cell is 1.6 THz.

From Eq. (10), if the device with only a pair of balanced-electrodes, the total 3 dB bandwidth of 1.4 THz can be obtained.

$$f_{3dB} = \sqrt{\frac{1}{f_{tr}^{-2} + f_{RC}^{-2}}} \tag{10}$$

The bandwidth here is remarkably large, which is due to the relatively small capacitance as a result of the nano-scale active region. When the device with N unit cells, f_{RC} is limited by the increased capacitance, decreased to 1.6/N THz. Therefore, the bandwidth of the GPD will be limited mainly by RC delay because the transit time limited bandwidth is much larger. For instance, when N is designed as 10, the bandwidth of the device is around 160 GHz and the length is around 5 μm.

It is well known that coherent technology can amplify a weak signal by using a high P_{LO}. In our case, if we consider the coherent gain of the signal due to a high P_{LO}, the effective responsivity R_{eff} can be used to describe the responsivity of the proposed device. Due to the quantum efficiency is relevant to the absorption of the active material, the effective responsivity R_{eff} can be given by

$$R_{eff} = \frac{I_{out}}{P_S} = M\,\eta_e \frac{e}{hv} = M\,\eta_i \eta_A \frac{e}{hv} \tag{11}$$

where $M = P_{LO}/P_S + 1$ is the coefficient for calculation, e is the unit charge, h is the Plank constant, v is the optical frequency, η_e, η_i and η_A are the external quantum efficiency (the number of charge carriers collected per incident photon), the internal quantum efficiency (the number of carriers collected per absorbed photons) and the absorption efficiency of the active material, respectively. Here, the absorption efficiency η_A is the differential absorptance η_d of the device. Considering the values of internal quantum efficiency $\eta_i = 15-30\%$ on metal/graphene interfaces [22],If we assume that the internal quantum efficiency is a maximum value of 30%, the effective responsivity of the device with 10 unit cells versus the P_{LO}/P_S ratio can be calculated, as shown in Fig. 8. From Fig. 8, it is shown when the P_{LO}/P_S ratio is from 20 dB to 30 dB, the effective responsivity increases accordingly, whose value changes in the range of 1 A/W to 4 A/W, which is much larger than that of the typical GPDs.

5. Conclusion

In summary, we present a novel scheme to integrate an optical hybrid based on standing wave with graphene-based SDPD for coherent detection. The proposed device has obvious advantages of low-complexity, ultracompact, fast response over a broad spectral range and CMOS compatibility. Utilizing a coherent mechanism of standing wave, the optical hybrid can be implemented in an SOI strip waveguide. By adopting a symmetric metallization scheme to utilize the mirror symmetry of the internal electric-field profile, the GPD with balanced-electrodes can realize self-balanced photodetection. Compare to the MMI optical hybrids connected to the conventional BPDs, our scheme can effectively reduce the complexity of coherent receiver and meet future demand for bandwidth. The light absorption properties have been discussed for demonstrating the operation feasibility. In the case of the device with 10 unit cells, the bandwidth is estimated to be 160 GHz and the length is around 5 μm. And the effective responsivity changes in the range of 1 A/W to 4 A/W when the P_{LO}/ P_S ratio is from 20 dB to 30 dB. The platform of graphene integrated silicon photonics promises small-form-factor and low-cost photonic devices for future high-speed large-scale chip-integration [45]. In addition, the scheme could also be extended to other substrate platforms and nano-scale PDs, revealing the potential and flexibility for high performance coherent detection in more areas.

References

[1] G. Li, "Recent advances in coherent optical communication," *Adv. Opt. Photon.*, vol. 1, no. 2, pp. 279–307, 2009.
[2] K. Roberts, D. Beckett, D. Boertjes, J. Berthold, and C. Laperle, "100G and beyond with digital coherent signal processing," *IEEE Commun. Mag.*, vol. 48, no. 7, pp. 62–69, Jul. 2010.
[3] M. Lu *et al.*, "Monolithic integration of a high-speed widely tunable optical coherent receiver," *IEEE Photon. Technol.*, vol. 25, no. 11, pp. 1077–1080, Jun. 2013.
[4] C. R. Doerr *et al.*, "Monolithic InP dual-polarization and dual-quadrature coherent receiver," *IEEE Photon. Technol.*, vol. 23, no. 11, pp. 694–696, Jun. 2011.
[5] R. J. Deri *et al.*, "Ultracompact monolithic integration of balanced, polarization diversity photodetectors for coherent lightwave receivers," *IEEE Photon. Technol.*, vol. 4, no. 11, pp. 1238–1240, Nov. 1992.
[6] D. Po, L. Xiang, S. Chandrasekhar, L. L. Buhl, R. Aroca, and C. Young-Kai, "Monolithic silicon photonic integrated circuits for compact 100+ Gb/s coherent optical receivers and transmitters," *IEEE J. Sel. Topics Quantum Electron.*, vol. 20, no. 4, pp. 150–157, Jul./Aug. 2014.
[7] P. Dong, C. Xie, and L. L. Buhl, "Monolithic polarization diversity coherent receiver based on 120-degree optical hybrids on silicon," *Opt. Exp.*, vol. 22, no. 2, pp. 2119–25, Jan. 2014.
[8] C. R. Doerr *et al.*, "Packaged monolithic silicon 112-Gb/s coherent receiver," *IEEE Photon. Technol.*, vol. 23, no. 12, pp. 762–764, Jun. 2011.
[9] C. R. Doerr *et al.*, "Monolithic polarization and phase diversity coherent receiver in silicon," *J. Lightw. Technol.*, vol. 28, no. 4, pp. 520–525, Feb. 2010.
[10] Y. Painchaud *et al.*, "Ultra-compact coherent receiver based on hybrid integration on silicon," in *Proc. Opt. Fiber Commun. Conf. Expo. Nat. Fiber Opt. Eng. Conf.*, 2013, Paper OM2J.2.
[11] Y. Kurata *et al.*, "Silica-based PLC with heterogeneously-integrated PDs for one-chip DP-QPSK receiver," *Opt. Exp.*, vol. 20, no. 26, pp. B264–B269, Dec. 2012.
[12] T. Ohyama *et al.*, "All-in-One 112-Gb/s DP-QPSK optical receiver front-end module using hybrid integration of silica-based planar lightwave circuit and photodiode arrays," *IEEE Photon. Technol.*, vol. 24, no. 8, pp. 646–648, Apr. 2012.
[13] J. Wang *et al.*, "Dual-quadrature coherent receiver for 100G Ethernet applications based on polymer planar lightwave circuit," *Opt. Exp.*, vol. 19, no. 26, pp. B166–B172, Dec. 12, 2011.
[14] K. S. Novoselov, V. I. Fal'ko, L. Colombo, P. R. Gellert, M. G. Schwab, and K. Kim, "A roadmap for graphene," *Nature*, vol. 490, no. 7419, pp. 192–200, Oct. 2012.
[15] F. Bonaccorso, Z. Sun, T. Hasan, and A. C. Ferrari, "Graphene photonics and optoelectronics," *Nature Photon.*, vol. 4, no. 9, pp. 611–622, 2010.
[16] M. Liu *et al.*, "A graphene-based broadband optical modulator," *Nature*, vol. 474, no. 7349, pp. 64–67, Jun. 2011.
[17] L. Abdollahi Shiramin and D. Van Thourhout, "Graphene modulators and switches integrated on silicon and silicon nitride waveguide," *IEEE J. Sel. Topics Quantum Electron.*, vol. 23, no. 1, pp. 94–100, Jan./Feb. 2017.
[18] C. Qiu, W. Gao, R. Vajtai, P. M. Ajayan, J. Kono, and Q. Xu, "Efficient modulation of 1.55 mum radiation with gated graphene on a silicon microring resonator," *Nano Lett.*, vol. 14, no. 12, pp. 6811–6815, Dec. 2014.
[19] Q. Bao and K. P. Loh, "Graphene photonics, plasmonics, and broadband optoelectronic devices," *ACS Nano*, vol. 6, no. 5, pp. 3677–3694, May 2012.
[20] K. F. Mak, M. Y. Sfeir, Y. Wu, C. H. Lui, J. A. Misewich, and T. F. Heinz, "Measurement of the optical conductivity of graphene," *Phys. Rev. Lett.*, vol. 101, no. 19, Nov. 2008, Art. no. 196405.
[21] F. Xia, T. Mueller, Y. M. Lin, A. Valdes-Garcia, and P. Avouris, "Ultrafast graphene photodetector," *Nature Nanotechnol.*, vol. 4, no. 12, pp. 839–843, Dec. 2009.

[22] T. Mueller, F. Xia, and P. Avouris, "Graphene photodetectors for high-speed optical communications," *Nature Photon.*, vol. 4, no. 5, pp. 297–301, 2010.
[23] X. Gan *et al.*, "Chip-integrated ultrafast graphene photodetector with high responsivity," *Nature Photon.*, vol. 7, no. 11, pp. 883–887, 2013.
[24] X. An, F. Liu, Y. J. Jung, and S. Kar, "Tunable graphene-silicon heterojunctions for ultrasensitive photodetection," *Nano Lett.*, vol. 13, no. 3, pp. 909–916, Mar. 13, 2013.
[25] X. Wang, Z. Cheng, K. Xu, H. K. Tsang, and J.-B. Xu, "High-responsivity graphene/silicon-heterostructure waveguide photodetectors," *Nature Photon.*, vol. 7, no. 11, pp. 888–891, 2013.
[26] A. Pospischil *et al.*, "CMOS-compatible graphene photodetector covering all optical communication bands," *Nature Photon.*, vol. 7, no. 11, pp. 892–896, 2013.
[27] C. H. Liu, Y. C. Chang, T. B. Norris, and Z. Zhong, "Graphene photodetectors with ultra-broadband and high responsivity at room temperature," *Nature Nanotechnol.*, vol. 9, no. 4, pp. 273–378, Apr. 2014.
[28] L. Xiang, Y. Xu, Y. Yu, and X. Zhang, "An ultracompact DP-QPSK demodulator based on multimode interference and photonic crystals," *J. Lightw. Technol.*, vol. 30, no. 11, pp. 1595–1601, Jun. 2012.
[29] Y. Painchaud, M. Poulin, M. Morin, and M. Têtu, "Performance of balanced detection in a coherent receiver," *Opt. Exp.*, vol. 17, no. 5, pp. 3659–3672, 2009.
[30] M.-S. Kwon, "Discussion of the epsilon-near-zero effect of graphene in a horizontal slot waveguide," *IEEE Photon. J.*, vol. 6, no. 3, 2014, Art. no. 6100309.
[31] X. Hu and J. Wang, "Ultrabroadband compact graphene-silicon TM-pass polarizer," *IEEE Photon. J.*, vol. 9, no. 2, Apr. 2017, Art. no. 7101310.
[32] E. D. Palik, *Handbook of Optical Constants of Solids I*. New York, NY, USA: Academic, 1985.
[33] E.D. Palik, *Handbook of Optical Constants of Solids II*. New York, NY, USA: Academic, 1991.
[34] E.D. Palik, *Handbook of Optical Constants of Solids III*. New York, NY, USA: Academic, 1998.
[35] J. Q. Wang *et al.*, "Graphene photodetector integrated on silicon nitride waveguide," *J. Appl. Phys.*, vol. 117, no. 14, 2015, Art. no. 144504.
[36] J. Q. Wang *et al.*, "High-responsivity graphene-on-silicon slot waveguide photodetectors," *Nanoscale*, vol. 8, no. 27, pp. 13206–13211, 2016.
[37] K. J. Tielrooij *et al.*, "Hot-carrier photocurrent effects at graphene-metal interfaces," *J. Phys. Condens. Matter*, vol. 27, no. 16, 2015, Art. no. 164207.
[38] D. Sun *et al.*, "Ultrafast hot-carrier-dominated photocurrent in graphene," *Nature Nanotechnol.*, vol. 7, no. 2, pp. 114–118, Jan. 2012.
[39] G. Konstantatos *et al.*, "Hybrid graphene-quantum dot phototransistors with ultrahigh gain," *Nature Nanotechnol.*, vol. 7, no. 6, pp. 363–368, May 2012.
[40] W. Xu *et al.*, "Chip-integrated nearly perfect absorber at telecom wavelengths by graphene coupled with nanobeam cavity," *Opt. Lett.*, vol. 40, no. 14, pp. 3256–3259, Jul. 2015.
[41] Y. Liu *et al.*, "Plasmon resonance enhanced multicolour photodetection by graphene," *Nature Commun.*, vol. 2, pp. 579, Dec. 2011.
[42] S. Camatel and V. Ferrero, "Homodyne coherent detection of ASK and PSK signals performed by a subcarrier optical phase-locked loop," *IEEE Photon. Technol.*, vol. 18, no. 1, pp. 142–144, Jan. 2006.
[43] S. Tsukamoto *et al.*, "Coherent demodulation of optical multilevel phase-shift-keying signals using homodyne detection and digital signal processing," *IEEE Photon. Technol.*, vol. 18, no. 10, pp. 1131–1133, May 2006.
[44] K. Kato, S. Hata, K. Kawano, and A. Kozen, "Design of ultra-wide band, high sensitivity p–i–n photodetectors," *IEICE Trans. Electron.*, vol. 76, no. 2, pp. 214–221, 1993.
[45] K. Kim, J. Y. Choi, T. Kim, S. H. Cho, and H. J. Chung, "A role for graphene in silicon-based semiconductor devices," *Nature*, vol. 479, no. 7373, pp. 338–344, Nov. 2011.